

OPEN ACCESS

Simulation-Based Investigation on Thermal Propagation in Li-ion Battery Modules with Regard to the Thermal Management System

To cite this article: Niklas Weber *et al* 2024 *J. Electrochem. Soc.* **171** 110516

View the [article online](#) for updates and enhancements.

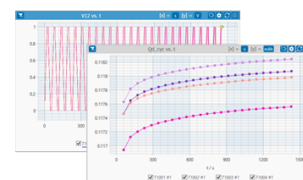
You may also like

- [Review—Understanding Thermal Runaway in Lithium-Ion Batteries: Trigger, Mechanism, and Early Warning Strategies](#)
Chenchen Liu, Hai Dai, Danyang Wang et al.
- [Recent Advances in Perovskite Nanomaterials for Sensing Applications](#)
Samiksha Dabas, Manish Kumar, Dharm Veer Singh et al.
- [Novel SoC-Based FBG Calibration Method for Decoupled Temperature and Strain Analysis within LIB Cells](#)
Christopher Schwab, Lea Leuthner and Anna Smith

PAT-Tester-x-8 Potentiostat: Modular Solution for Electrochemical Testing!

EL-CELL®
electrochemical test equipment

- ✓ **Flexible Setup with up to 8 Independent Test Channels!**
Each with a fully equipped Potentiostat, Galvanostat and EIS!
- ✓ **Perfect Choice for Small-Scale and Special Purpose Testing!**
Suited for all 3-electrode, optical, dilatometry or force test cells from EL-CELL.
- ✓ **Complete Solution with Extensive Software!**
Plan, conduct and analyze experiments with EL-Software.
- ✓ **Small Footprint, Easy to Setup and Operate!**
Usable inside a glove box. Full multi-user, multi-device control via LAN.



Contact us:

☎ +49 40 79012-734

✉ sales@el-cell.com

🌐 www.el-cell.com



Simulation-Based Investigation on Thermal Propagation in Li-ion Battery Modules with Regard to the Thermal Management System

Niklas Weber,^{1,z} Christian Michel,¹ Sebastian Schuhmann,² Jens Tübke,² and Hermann Nirschl¹

¹Institute of Mechanical Process Engineering and Mechanics, Karlsruhe Institute of Technology, 76131 Karlsruhe, Germany

²Fraunhofer Institute for Chemical Technology ICT, 76327 Pfinztal, Germany

Thermal propagation in Li-ion battery systems is affected by a wide range of influencing factors including chemical cell properties as well as thermal transport phenomena. Due to the dependence on thermal surroundings it is crucial to regard the entire battery system including peripheral components when assessing thermal runaway and propagation risks. This study proposes a simulation-based approach to support design and dimensioning of potential safety measures. It is based on a chemical model for the thermal runaway decomposition reactions combined with 3D thermal simulations. This is applied on exemplary ten cell battery pack in order to investigate on effects on heat transfer during thermal propagation. Insulation and cooling systems are included in the simulation environment for that purpose. It is found that propagation behavior significantly depends on their positioning within in pack and on thermal boundary conditions. Placing too many barriers may exacerbate hazardous situations instead of mitigating them due to heat accumulation effects. Cooling systems are shown to be able to support thermal runaway mitigation strategies but their effectiveness is limited by thermal transport inside the battery cells.

© 2024 The Author(s). Published on behalf of The Electrochemical Society by IOP Publishing Limited. This is an open access article distributed under the terms of the Creative Commons Attribution 4.0 License (CC BY, <http://creativecommons.org/licenses/by/4.0/>), which permits unrestricted reuse of the work in any medium, provided the original work is properly cited. [DOI: 10.1149/1945-7111/ad9351]



Manuscript submitted August 19, 2024; revised manuscript received September 24, 2024. Published November 25, 2024.

In Li-ion battery systems, the most severe safety incidents arise from the uncontrolled decomposition reactions of a cell, causing massive heat and gas release. This is called thermal runaway. Without proper countermeasures, thermal propagation happens.¹⁻³ It is defined as the “sequential occurrence of thermal runaway within a battery system triggered by thermal runaway of a cell in that battery system”.⁴ Cell spacing and thermal insulation between cells and modules have been established as strategies to prevent or mitigate thermal propagation.⁵⁻⁷ The goal is to achieve a safe battery system, but safety measures add further mass and volume which lowers the energy density at pack level. Therefore, pack designers strive to minimize the volume and mass of the safety system by designing it as efficient as possible. Potentially, the safety measures can be supported by heat withdrawal through the thermal management system (TMS) of the battery pack.^{8,9}

The main purposes of a TMS however are to keep the temperature of the battery cells in the optimal operating window, usually around 15 °C–35 °C for Li-ion batteries,¹⁰ and to keep the temperature gradients within the battery pack low to provide the same working conditions for all batteries in the pack. Under these circumstances the batteries work most efficiently, aging is minimized and any thermal hazards to the battery are prevented.^{11,12} Besides fulfilling these purposes, several other factors influence the design of the TMS. These include energy consumption and additional mass of the TMS as well as economic reasons such as engineering complexity and cost. Due to the individual nature of each battery pack a large variety of different TMS has been developed based on the named requirements.^{10,13,14}

The main differentiation among the TMS is the cooling agent which is usually either the ambient air or a liquid coolant.^{13,15} Passive air cooling fully relies on natural convection while active air cooling systems apply an additional fan in order to enhance the air flow rate and thus the heat transfer coefficient. In liquid cooled battery systems, the cells can be in direct contact with the cooling agent which is called direct or immersion cooling.^{16,17} For indirect liquid cooling, plates with flow channels are used. These are either placed between the battery cells or on bottom or the terminals of the cells. Water-glycol-mixtures and pure water are the most common

cooling agents for indirect cooling. For direct cooling, a dielectric liquid is required in order to prevent shortcuts.¹⁸

The TMS is designed to maintain optimal working conditions for the battery system during regular charging and discharging processes. However, it also takes effect in hazardous situations, namely when one or more cells in the battery system undergo thermal runaway. In these situations, the TMS can help to prevent thermal propagation of the hazardous event. Several authors have investigated how a cooling system can effectively synergize with safety measures such as thermal barriers to mitigate the effect of a thermal runaway.^{8,19,20} Rui et al. have shown that a higher rate of heat dissipation via cooling effectively reduces the thickness of barriers needed for stopping thermal propagation.⁸

Each battery system has its individual properties and requirements, which affect the design of the safety system. On cell level, this includes the cell type (usually pouch, cylindrical or prismatic) as well as the chemistry and inner buildup of the cells.^{21,22} On module or system level, the arrangement of cells and other components, the shape of the battery system, thermal boundary conditions and confining pressure are to be regarded.^{23,24} All these battery system properties impact heat generation, accumulation and transport in hazardous thermal runaway situations with direct effect on thermal propagation behavior.

Due to the large parameter space, this work proposes a simulation-based approach to the design and arrangement optimization of the battery pack’s safety system while taking the TMS into account. For this purpose, a 3D simulation setup is used which was developed and validated in our previous publications.^{25,26} It features a chemical model for the degradation reaction of the cell components and combines it with a homogenized thermal battery model. It further takes the effect of gas generation on the thermal transport inside the battery cells into account. This simulation environment is applied on a reference battery system in order to derive general statements about thermal propagation prevention and propagation times in dependence of the named influences.

Model Description

Chemical model.—During the thermal runaway of Li-ion batteries, various decomposition reactions take place that lead to the release of large quantities of heat and gas. Since it is not feasible to include all possible thermal runaway reactions due to the computational effort involved, ten representative reactions were selected and

^zE-mail: niklas.weber@kit.edu

Table I. Summary of chemical reactions used in the model.

No.	Description	Chemical equation
R1	Anode main reaction	$2 \text{LiC}_6 + \text{C}_3\text{H}_4\text{O}_3 \rightarrow \text{Li}_2\text{CO}_3 + \text{C}_2\text{H}_4 + 2 \text{C}_6$
R2	LiF formation	$\text{Li}_2\text{CO}_3 + \text{PF}_5 \rightarrow 2 \text{LiF} + \text{POF}_3 + \text{CO}_2$
R3	Li ₂ O formation	$\text{Li}_2\text{CO}_3 \rightarrow \text{Li}_2\text{O} + \text{CO}_2$
R4	Cathode, full oxidation	$5 \text{MO}_2 + \text{C}_3\text{H}_4\text{O}_3 \rightarrow 5 \text{MO} + 3 \text{CO}_2 + 2 \text{H}_2\text{O}$
R5	Cathode, partial oxidation	$5 \text{MO}_2 + 3 \text{C}_3\text{H}_4\text{O}_3 \rightarrow 5 \text{MO} + 6 \text{CO} + 4 \text{H}_2 + 3 \text{CO}_2 + 2 \text{H}_2\text{O}$
R6	Salt decomposition	$\text{LiPF}_6 \rightarrow \text{LiF} + \text{PF}_5$
R7	Solvent decomposition	$n \text{C}_3\text{H}_4\text{O}_3 \rightarrow (\text{CH}_2\text{CH}_2\text{O})_n + n \text{CO}_2$
R8	Solvent evaporation	$\text{C}_3\text{H}_4\text{O}_3 (\text{l}) \rightarrow \text{C}_3\text{H}_4\text{O}_3 (\text{g})$
R9	HF formation	$\text{POF}_3 + 3 \text{H}_2\text{O} \rightarrow 3 \text{HF} + \text{H}_3\text{PO}_4$
R10	Water gas shift	$\text{CO} + \text{H}_2\text{O} \rightleftharpoons \text{CO}_2 + \text{H}_2$

are listed in Table I. This chemical reaction system was first presented in our previous work.²⁵ The main contributors to heat release during thermal runaway are the reaction of intercalated lithium with electrolyte solvent on the anode side (reaction R1) and the cathode decomposition which is represented by reactions R4 and R5.^{27,28} During composition of the metal oxide cathode, oxygen is released and reacts with electrolyte solvent in a partial or full oxidation reaction. Reaction R1 is also the main source of released gaseous hydrocarbons and reactions R4 and R5 are mostly responsible for the liberation of CO₂, CO, H₂O and H₂. As electrolyte solvent is an important reactant in reactions R1, R4 and R5, its depletion via other reactions becomes meaningful as well.²⁹ Therefore, reactions R7 and R8 are included. Reaction R7 describes the self decomposition of electrolyte solvent which forms a polymeric product.^{30,31} Reaction R8 is the evaporation of the organic solvent.

Reactions R2 and R3 are the further reactions of lithium carbonate which originates from the anode main reaction R1. Lithium oxide and lithium fluoride are the products of these reactions which are the main species on the anode surface at high temperatures.³² Further, these reactions contribute to the gas formation of CO₂ and fluorine containing species. The production of these species is facilitated by reaction R6, the decomposition of the conductive salt LiPF₆. Since Li-ion batteries are widely reported to release hydrogen fluoride as the main fluorine containing gas,^{33,34} reaction R9 is included which converts POF₃ to HF. Finally, the water gas shift reaction R10 is necessary in order to predict the gas composition correctly.

For all ten reactions the reaction rates are calculated by the power law, given by Eq. 1.

$$r_i = k_i \prod_j x_j^{a_{j,i}} \quad [1]$$

k_i , x_j and $a_{j,i}$ are the reaction constant of reaction i the mass fraction of species j and the according exponent for reaction i . The reaction rates are then used to update the mass fractions of all species according to Eq. 2 with the stoichiometric coefficients $\nu_{i,j}$ of species j in reaction i .

$$\frac{dx_j}{dt} = \sum_i \nu_{i,j} r_i \quad [2]$$

The calculation of the initial mass fractions is described in detail in Section "Battery properties". For determining the temperature dependent reaction constants k_i the Arrhenius approach is used for all reactions except for the anode main reaction R1:

Table II. Reaction enthalpies of the ten chemical reactions and the according references. Please note that we set the reaction enthalpy of R7 to 0 as no literature values could be found for the polymeric product and the impact on heat generation is negligible.

No.	Description	Reaction Enthalpy	References
R1	Anode main reaction	$-281.4 \text{ kJ mol}^{-1}$	29
R2	LiF formation	$-77.1 \text{ kJ mol}^{-1}$	29, 36, 37
R3	Li ₂ O formation	$222.6 \text{ kJ mol}^{-1}$	29, 38
R4	Cathode, full oxidation	$-201.5 \text{ kJ mol}^{-1}$	39, 40
R5	Cathode, partial oxidation	$-105.5 \text{ kJ mol}^{-1}$	39, 40
R6	Salt decomposition	$84.27 \text{ kJ mol}^{-1}$	37
R7	Solvent decomposition		
R8	Solvent evaporation	60.8 kJ mol^{-1}	29
R9	HF formation	$-123.4 \text{ kJ mol}^{-1}$	36, 41
R10	Water gas shift	$-41.2 \text{ kJ mol}^{-1}$	36

$$k_i = A_i \exp\left(-\frac{E_i}{RT}\right) \quad [3]$$

where A_i is the pre-exponential constant and E_i is the activation energy of reaction i . R and T are the universal gas constant and the local temperature. The anode main reaction is inhibited by the deposition of lithium salts on the surface which are formed by reactions R1, R2 and R3. This is regarded by an exponential term in Eq. 4 where z is a dimensionless measure for the amount of deposited salts. In accordance with the model published by Shurtz et al.²⁹ z has an upper limit z_{crit} which also limits the inhibition effect of the salts.

$$k_i = A_i \exp\left(-\frac{E_i}{RT}\right) \exp(-z) \quad [4]$$

Thermal model.—The chemical model is coupled with a thermal simulation via a source term in the 3D fourier equation which is given by Eq. 5.³⁵

$$\rho c_p \frac{\partial T}{\partial t} = \lambda_{\perp} \frac{\partial^2 T}{\partial x^2} + \lambda_{\parallel} \frac{\partial^2 T}{\partial y^2} + \lambda_{\parallel} \frac{\partial^2 T}{\partial z^2} + \dot{q} \quad [5]$$

ρ and c_p are density and heat capacity and \dot{q} is the chemical source term. λ is the thermal conductivity. As Eq. 5 implies, the battery cell's thermal conductivity is non-isotropic due to its layered structure. λ_{\perp} is the thermal conductivity perpendicular to the electrode and separator sheets and λ_{\parallel} parallel to the sheets. This is described in further detail in Section "Battery properties". The chemical source term \dot{q} is computed with the reaction rates, calculated by Eq. 1 and the reaction enthalpies, given in Table II.

$$\dot{q}_B = \sum_k r_k \Delta H_{r,k} \quad [6]$$

In all non-battery regions, Eq. 5 is applied with a isotropic thermal conductivity and no heat source term except for the cooling regions. The source term for the cooling regions is described in Section "Cooling system model".

For initializing the thermal runaway and propagation process, one cell in the battery pack is triggered. For this purpose, an additional heat source is applied to the chosen battery cell. It corresponds to heating rate of 40 Kmin⁻¹ and is uniformly distributed over the entire battery cell. This represents an arbitrary trigger mechanism as the focus of this work is propagation of thermal runaway rather than initiation.

On the boundary of the battery pack, heat transfer to the surroundings via convection and radiation is to be considered. The heat flux on the boundaries \dot{q}_{BC} is calculated according to Eq. 7.

$$\dot{q}_{BC} = h(T_{BC} - T_s) + \sigma \epsilon (T_{BC}^4 - T_s^4) \quad [7]$$

ϵ and σ are the emissivity and the Stefan-Boltzmann constant. T_{BC} and T_s are the temperatures of the test rig on the boundary and the surroundings respectively and h is the convective heat transfer coefficient.

Battery properties.—For computing the cell properties, a homogenized battery model is used. The layers of the battery cell such as electrode sheets, current collectors and separators are not simulated as individual regions; instead the properties are averaged over the entire battery cell. The required input for the presented models includes thermal properties such as thermal conductivity, density and heat capacity as well as the initial chemical composition. In this work, we consider different types of batteries. They differ in their inner buildup: the number n_i , thickness s_i and porosity ϵ_i of the electrode sheets. These parameters usually mark the difference between high energy and high power cells when the cell chemistry is identical.^{42,43} The battery cells modeled in this work contain graphite anodes, NMC622 cathodes and LP30 electrolyte (1M LiPF6 in EC/DMC 50:50 wt%). The first step to determine the battery properties from these values is to calculate the total volume of each battery component.

$$V_i = n_i s_i F_i (1 - \epsilon_i) (1 - \gamma_i) \quad [8]$$

F_i is the surface of sheet i . For the active material layers, an additional factor $(1 - \gamma_i)$ is introduced where γ_i is the volume fraction of other components like binder and additives within the active material layers. In all other layers $\gamma_i = 0$. With the volumes V_i of each component calculated and the individual densities ρ_i given, the average density is computed with Eq. 9.

$$\bar{\rho} = \frac{\sum_i V_i \rho_i}{\sum_i V_i} \quad [9]$$

And the mass fractions x_i are given by

$$x_i = \frac{V_i \rho_i}{\sum_j V_j \rho_j} \quad [10]$$

As mentioned in Section "Thermal model" the thermal conductivity of the battery cells is non-isotropic. It is determined in direction perpendicular and parallel to the electrode sheets by Eqs. 11 and 12 respectively.⁴⁴

$$\lambda_{\perp} = \frac{\sum_i n_i s_i}{\sum_i \frac{n_i s_i}{\lambda_i}} \quad [11]$$

$$\lambda_{\parallel} = \frac{\sum_i n_i s_i \lambda_i}{\sum_i n_i s_i} \quad [12]$$

Since pouch cells do not have a rigid housing, the gases produced during thermal runaway reactions cause the pouch bag to inflate, which has a major impact on the thermal transport behavior.⁴⁵ In our previous work, we developed a multi-stage model that couples the cell internal gas generation with the thermal resistance of the battery.²⁶ The simplifying modeling assumption is that gas forms layers with uniform thickness. In direction parallel to the sheets, thermal transport is governed by the highly conductive current collectors and the influence of gases can be neglected. In perpendicular direction however, gas generation causes additional thermal resistance which is expressed via Eq. 13.

$$R_{tot,\perp} = R_{B,\perp} + R_{gas} = \frac{s}{\lambda_{\perp}} + R_{gas} \quad [13]$$

where $R_{tot,\perp}$ is the total thermal resistance of the gas producing cell, $R_{B,\perp}$ the initial resistance of the battery stack, R_{gas} the thermal resistance of the produced gases and s the total thickness of the battery stack. R_{gas} is directly coupled with the amount of gas that has been produced n_{gas} which is obtained from the chemical model. The coupling between R_{gas} and n_{gas} is divided in four stages. In the first stage, up to approximately 100 °C, no gas is produced and thus, there is no influence on the heat transfer. The second stage describes the blow-up of the cell until the breakage of the pouch seam which marks the first venting event. R_{gas} increases linearly with the amount of produced gas.

After rapid thermal runaway, stage four is entered. No further gas is produced and again, there is no effect on heat transfer. The following Eqs. define the computation of R_{gas} in the four different stages:

$$R_{gas,1} = 0 \quad [14]$$

$$R_{gas,2} = \frac{n_{gas}}{n_{gas,Vent}} \cdot R_{gas,max} \quad [15]$$

$$R_{gas,3} = R_{const} \quad [16]$$

$$R_{gas,4} = 0 \quad [17]$$

The three modeling parameters are the maximum thermal resistance of the gases immediately before the first venting event $R_{gas,max}$, the amount of gas produced up to that point $n_{gas,Vent}$ and the gas thermal resistance in stage three $R_{gas,3}$. These are listed in Table III along with the other parameters of the battery model. The gas thermal resistance model has been described in further detail and validated in our previous work²⁶ to which we refer for further information.

For representing different cell types, ranging from high power to high energy cells, five exemplary cells were defined. They differ in number, thickness and porosity of the electrode sheets. These parameters are shown in Table IV. The thickness of the individual layers is chosen in a way, that the thickness of the entire battery stack is the same for all cell types. Further, the outer geometry of the cells, the cell chemistry and the amount of electrolyte is identical as well. The overall properties of the batteries, used in the homogenized model, are calculated according to Eqs. 8 to 12. In all simulations where nothing else is stated, cell type 3 is used.

Cooling system model.—Besides the battery cells, other components of the battery pack have to be considered in the simulation, especially the different thermal management systems. Air cooling is included via the thermal boundary condition given by Eq. 7. Passive air cooling needs no further adjustment of the boundary condition. Active air cooling impacts the heat transfer coefficient h due to forced convection caused by a fan. For liquid cooling, cooling plates are added to the system. Dependent on their position, either side cooling or edge cooling is applied. In this work, only edge cooling is employed by placing one cooling plate that contacts all battery cells at their bottom. In order to restrict the computation time, the coolant flow within the plates is not resolved in detail, but instead the plates are treated as solid regions with a volumetric heat sink \dot{q}_{cool} which is computed according to Eq. 18.

$$\dot{q}_{cool} = \frac{\dot{V}_c \rho_c c_{p,c}}{V_{plate}} (\min(T_{plate}, T_{c,boil}) - T_{c,0}) \quad [18]$$

where \dot{V}_c , ρ_c and $c_{p,c}$ are the volumetric flow rate, density and heat capacity of the coolant. $T_{c,0}$ is its initial temperature and $T_{c,boil}$ is its

Table III. Material properties of the battery components and modelling parameters. Some parameters are varied in this study. These are the default values which are used if nothing else is stated.

Description	Symbol	Value
Thermal conductivity cathode layer	λ_{cat}	0.65 Wm ⁻¹ K ⁻¹
Thermal conductivity anode layer	λ_{an}	1.02 Wm ⁻¹ K ⁻¹
Thermal conductivity positive current collector	λ_{pcc}	238 Wm ⁻¹ K ⁻¹
Thermal conductivity negative current collector	λ_{ncc}	398 Wm ⁻¹ K ⁻¹
Thermal conductivity separator	λ_{sep}	0.2 Wm ⁻¹ K ⁻¹
Thermal conductivity pouch bag	λ_{pouch}	0.32 Wm ⁻¹ K ⁻¹
Density cathode material	ρ_{cat}	4600 kg m ⁻³
Density anode material	ρ_{an}	2200 kg m ⁻³
Density separator	ρ_{sep}	2700 kg m ⁻³
Density positive current collector	ρ_{pcc}	2702 kg m ⁻³
Density negative current collector	ρ_{ncc}	8933 kg m ⁻³
Density pouch bag	ρ_{pouch}	1453 kg m ⁻³
Density electrolyte	ρ_{ele}	1260 kg m ⁻³
Volume electrolyte	V_{ele}	40 mL
Constant battery heat capacity	$c_{p,B}$	1300 Jkg ⁻¹ K ⁻¹
Thickness positive current collector	s_{pcc}	15 μ m
Thickness negative current collector	s_{ncc}	11 μ m
Thickness separator	s_{sep}	25 μ m
Thickness pouch bag	s_{pouch}	155 μ m
Porosity separator	ϵ_{sep}	0.5
Battery height	d_B	150 mm
Battery width	b_B	220 mm
Amount of gas produced before the first venting event	$n_{gas,vent}$	0.1473 molkg ⁻¹
Gas thermal resistance in stage 3	$R_{gas,3}$	0.0090 m ² K W ⁻¹
Maximum gas thermal resistance	$R_{gas,max}$	0.1017 m ² K W ⁻¹

boiling temperature at ambient pressure. V_{plate} and T_{plate} are the volume and the local temperature of the cooling plate.

As a simple modeling approach for the heat sink, we use a simple balance equation for the coolant and weight the heat sink according to the local temperatures of the cooling plate. However, we restrict the local heat sink by limiting the temperature difference to the difference of the boiling and the initial temperature of the coolant since it is unlikely that the cooling system yields ideal heat dissipation due to hindered heat transfer and potential damage to the cooling system when the boiling temperature of the coolant is exceeded.^{19,20} This modeling approach does not enable detailed assessment of the temperature distribution within the cooling plate, but it allows to investigate on the general influence of cooling plates on the thermal propagation behavior.

As materials for the cooling plate and fluid, we choose aluminum magnesium alloy with 3% magnesium and water respectively. Besides the actively cooled plates and the cells, the battery systems analyzed in this work contain insulating plates between the cells.

Table V. Thermal data of the cooling and insulation components.

Description	Symbol	Value
Liquid coolant density	ρ_c	997 kg m ⁻³
Liquid coolant heat capacity	$c_{p,c}$	4179 Jkg ⁻¹ K ⁻¹
Initial coolant temperature	$T_{c,0}$	25 °C
Coolant boiling temperature	$T_{c,boil}$	100 °C
Cooling plate thermal conductivity	λ_{plate}	128 Wm ⁻¹ K ⁻¹
Cooling plate density	ρ_{plate}	2667 kg m ⁻³
Cooling plate heat capacity	$c_{p,plate}$	869 Jkg ⁻¹ K ⁻¹
Insulation thermal conductivity	λ_{ins}	0.06 Wm ⁻¹ K ⁻¹
Insulation density	ρ_{ins}	750 kg m ⁻³
Insulation heat capacity	$c_{p,ins}$	900 Jkg ⁻¹ K ⁻¹

These are made of mica composite materials. The thermal data of the cooling and insulation components are given in Table V.

Simulation setup.—In order to investigate on the thermal propagation behavior, an exemplary Li-ion battery pack is considered. It consists of ten pouch cells and further cooling or insulating components. The number and positioning of insulations may vary between the simulations. For easier reference, the potential positions of the insulations are enumerated in the following. For example, position 1 refers to the position between the first two battery cells. The first battery cell is the cell on the rim of the battery pack in which thermal runaway is triggered first. A schematic drawing of the battery pack and the position numbers is displayed in Fig. 1. In some simulations, an additional cooling plate is integrated in the system. It is placed as a bottom plate below all battery cells and insulations.

A main measure for the assessment of the thermal propagation behavior of this battery pack is the propagation time. It is defined as the time increment between the thermal runaway times of two neighboring battery cells which may have a barrier between them. Since the evaluation of peak temperatures may be blurred by thermal transport effects, thermal runaway times are defined as the moment of maximum gas generation in the specific cell. All simulations were carried out with the open source software OpenFOAM.

Results and Discussion

Arrangement effects.—For the dimensioning of thermal barriers, it is crucial to investigate and understand effects on thermal propagation time and critical barrier thickness. For this purpose, a series of simulations on the ten cell battery pack described in Section "Simulation setup" has been conducted with only one thermal barrier. Figure 2 shows the propagation time at the barrier which is dependent on its position. When data points are missing, that means that thermal propagation is stopped at the barrier. The position number indicates after how many cells the barriers is placed, given that the trigger cell is on the rim of the battery pack. The test series was performed with three different barrier thicknesses: 1, 2 and 3 mm.

Table IV. Number, thickness and porosity of the electrode sheets of the five cell types. The total areal weight of the active material has been calculated for comparison of the cell types.

Cell type	Number		Thickness		Porosity		Areal weight	
	Anode	Cathode	Anode	Cathode	Anode	Cathode	Anode	Cathode
1	6	5	116.3 μ m	116.3 μ m	0.25	0.25	0.215 g cm ⁻²	0.350 g cm ⁻²
2	7	6	95.5 μ m	95.5 μ m	0.3	0.3	0.192 g cm ⁻²	0.321 g cm ⁻²
3	9	8	68.6 μ m	68.6 μ m	0.35	0.35	0.165 g cm ⁻²	0.286 g cm ⁻²
4	11	10	51.9 μ m	51.9 μ m	0.4	0.4	0.141 g cm ⁻²	0.249 g cm ⁻²
5	13	12	40.5 μ m	40.5 μ m	0.45	0.45	0.119 g cm ⁻²	0.214 g cm ⁻²

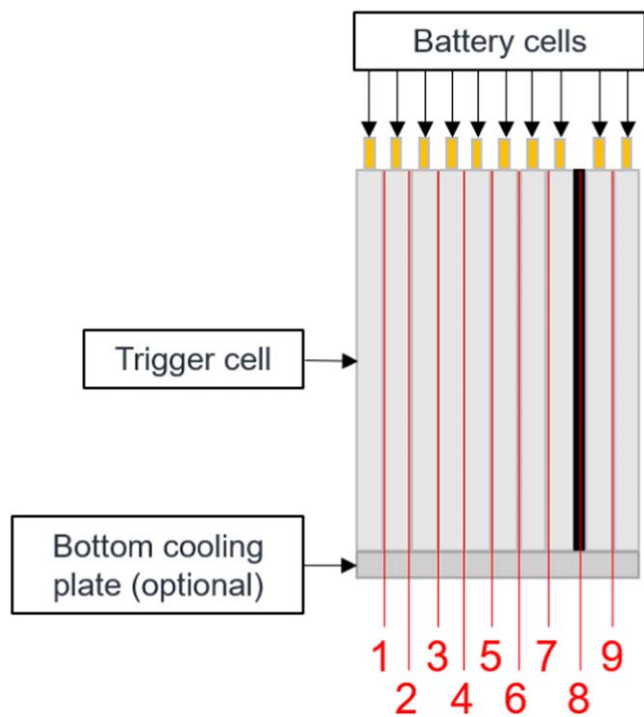


Figure 1. Schematic drawing of the simulated battery pack. The red lines and numbers indicate the enumeration of the barrier positioning. In this case a barrier is placed at position 8 as an example.

The results in Fig. 2 show that thermal propagation is not just defined by the thermal barrier and the two adjacent battery cells but thermal transport and accumulation effects in the surrounding cells play a major role as well. A 2 mm thermal barrier is only able to stop propagation when it is placed directly after the trigger cell and a 3 mm barrier stops propagation when placed up to the third position. It can be concluded that the necessary barrier thickness increases the more battery cells are placed before the thermal barrier. The reason for this is that the total ratio of heat dissipation and heat capacity of the cells placed before the barrier is diminished with a higher number of cells since middle cells have lower heat dissipation area than the trigger cell on the rim. Rui et al. have already proven that the prevention of thermal propagation is dependent on both heat dissipation and insulation.⁸ It is however also important to take the heat capacity into account in relation to the heat dissipation.

If the thermal propagation cannot be stopped by the barrier, its position still has a significant effect on the propagation time. The

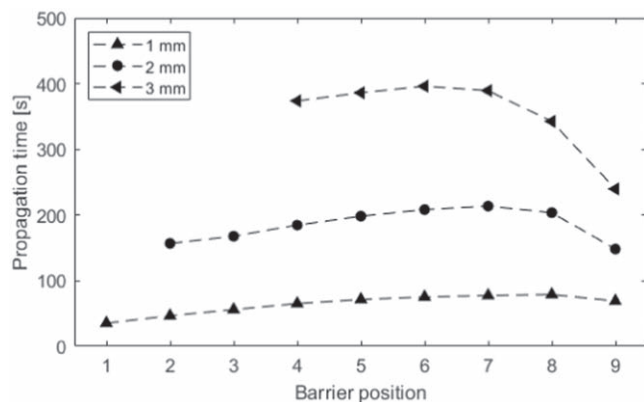


Figure 2. Dependence of the propagation time on the position of the thermal barrier within the stack for different barrier thicknesses. A missing data point indicates that the barrier stopped thermal propagation.

propagation time first rises with increasing barrier position until a maximum is reached followed by a sharp decrease toward position 9. The reason for the initial increase in propagation time is the following: if only few cells are placed before the barrier, they are heated to a higher temperature via heat conduction from the first cell. Since heat generation during thermal runaway is approximately the same, they also reach a higher peak temperature which leads into an increased temperature difference to the cell behind the barrier and thus into enhanced heat conduction. This causes a shorter propagation time if fewer cells are placed before the barrier. It is important to note that this effect is inherent in the thermal triggering method and may not occur with other triggering methods like nail penetration. Towards position 9 it is superposed by a heat accumulation effect that causes propagation times to drop. When there are only few battery cells behind the barrier, heat accumulates faster in the cell directly behind the barrier as the heat dissipation rate at the boundary is relatively low. This causes the lower propagation times when the barrier is at position 9. The superposition of the two named effects, heat accumulation and pre-heating, leads into a maximum of the propagation time at a certain position which depends on the barrier thickness. It is located at position 8 for 1 mm barriers, at position 7 for 2 mm barriers and at position 6 for 3 mm barriers.

For better visibility of the effect of barrier thickness on the propagation time, Fig. 3 shows this relation in greater detail. Compared to Fig. 2, we added further barrier thicknesses in steps of 0.5 mm. To keep the results and the figure comprehensible, we chose to only include the results for three barrier positions: positions 3, 6 and 9.

The results for all barrier positions show the expected increasing trend with the barrier thickness which has already been reported in literature.³ In position 3 and 6, the increase is approximately quadratic up to a thickness of 2.5 mm or 3 mm respectively. Generally, that means that few thick barriers yield a higher total propagation time than many thin barriers, given that the same total mass of insulating material is used. At position 3, the 3 mm barrier already stops thermal propagation. At position 6 the quadratic relation of barrier thickness and propagation time holds up to a thickness of 3 mm. For a barrier thickness of 3.5 mm, there is a severe deviation from this trend as the propagation time sharply increases to 1099 s compared to the 396 s at 3 mm barrier thickness. That implies that there is a massive further delay when the barrier thickness approaches the critical, thermal propagation stopping thickness.

At position 9, the initial increase in propagation time with the barrier thickness is almost linear. It can be concluded that the described heat accumulation effect reduces the dependence. Further, it is notable that the 0.5 mm barrier yields a higher propagation time at position 9 compared to positions 3 and 6. However, barriers thicker than 1.5 mm achieve a lower propagation time at position 9 compared to the other two positions. This emphasizes that the heat accumulation effect is more impactful with thicker barriers. With a barrier thickness of 3.5 mm, another sharp increase in propagation time can be observed as the critical barrier thickness is approached.

In order to further investigate on heat accumulation effects, further simulations with two thermal barriers were conducted. In these simulations, the first barrier is placed at position 3 and the second barrier is placed with a distance of 1, 2, 3 or 4 cells to the first barrier, so either at position 4, 5, 6 or 7. As Fig. 2 demonstrates, a 3 mm barrier at position 3 stops thermal propagation if no second barrier is placed in the stack. The purpose is to find out whether an additional barrier can cause thermal propagation over the 3 mm barrier which is indicated in Table VI.

The results show that a second 3 mm barrier at position 4 or 5 causes thermal propagation at the first barrier due to heat accumulation. If the second barrier is placed at position 4, thermal propagation is stopped at this second barrier. If the second barrier is placed at position 4, thermal runaway propagates through the entire battery pack.

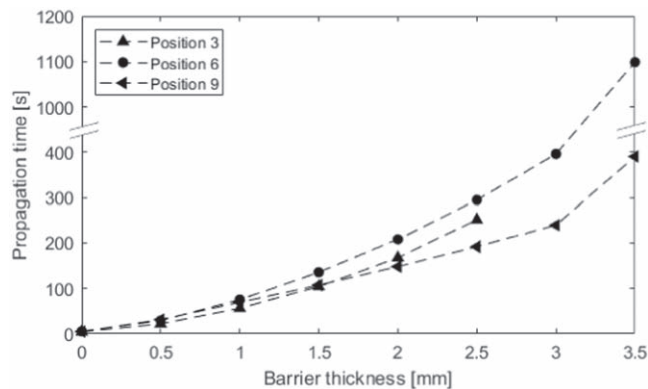


Figure 3. Effect of the barrier thickness on the propagation time for barrier positions 3, 6 and 9. A barrier thickness of 0 means that no barrier has been applied. A missing data point indicates that the barrier stopped thermal propagation.

Table VI. Indication whether thermal propagation occurs at the barrier at position 3 in the two barrier simulations. The second barrier is placed at the position given in the table. Barrier thicknesses of 3 mm and 4 mm were applied.

Barrier thickness	Pos. 4	Pos. 5	Pos. 6	Pos. 7
3 mm	Yes	Yes	No	No
4 mm	Yes	No	No	No

Even if 4 mm barriers are applied, thermal propagation is not stopped by the barrier at position 3 if there is only one battery cell between the two barriers. Again, this underlines that few thick barriers are more efficient at mitigating and stopping thermal propagation than many thin barriers since too many barriers enhance heat accumulation effects.

Interplay of safety measures with the cooling system.—Active air cooling systems temper the battery pack by applying forced convection. As described in Section "Cooling system model", this affects the heat transfer coefficient h at the boundary of the battery pack. Apart from that, the buildup of the battery pack is kept the same and thus, it is represented by Fig. 1. Figure 4 displays the effect of the heat transfer coefficient on the propagation time for different barrier positions. Note that the curve for $h = 5 \text{ W m}^{-2} \text{ K}^{-1}$ is identical to the curve for a barrier thickness of 2 mm in Fig. 2 since we kept the barrier thickness constant at 2 mm in this part of the study. The heat transfer coefficient is varied between $h = 5 \text{ W m}^{-2} \text{ K}^{-1}$ which marks natural convection and $h = 150 \text{ W m}^{-2} \text{ K}^{-1}$. This is well in range that Feng et al. report for active air cooling systems.⁴⁶

Obviously, there is a tendency of increasing propagation time with a rising heat transfer coefficient as heat dissipation is enhanced. Additionally, with $h = 100 \text{ W m}^{-2} \text{ K}^{-1}$ thermal propagation is stopped by the 2 mm barrier at position 2 and with $h = 150 \text{ W m}^{-2} \text{ K}^{-1}$ it is stopped if the barrier is at position 2 or 3. The enhanced heat dissipation also affects the heat accumulation effect, described in Section "Arrangement effects", which causes the propagation time to drop toward position 9. It is apparent that the drop in propagation time between position 8 and 9 is lower the higher the heat transfer coefficient is. The improved heat transfer at the boundary prevents heat to accumulate as fast as it does with lower heat transfer coefficients. For the highest heat transfer coefficient $h = 150 \text{ W m}^{-2} \text{ K}^{-1}$, this effect is even reverted as the dissipated heat flux at the boundary is bigger than the conducted heat flux to the neighbor cells is in cases with multiple cells behind the barrier. Therefore, the propagation time is highest at position 9 in that case.

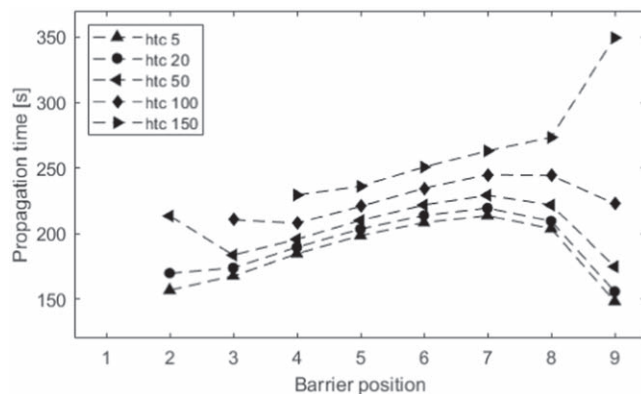


Figure 4. Propagation time over barrier position with heat transfer coefficients (htc) ranging from 5 to $150 \text{ W m}^{-2} \text{ K}^{-1}$. The enhanced outer heater transfer coefficient represents active air cooling. The barrier thickness is 2 mm in all cases. A missing data point indicates that the barrier stopped thermal propagation.

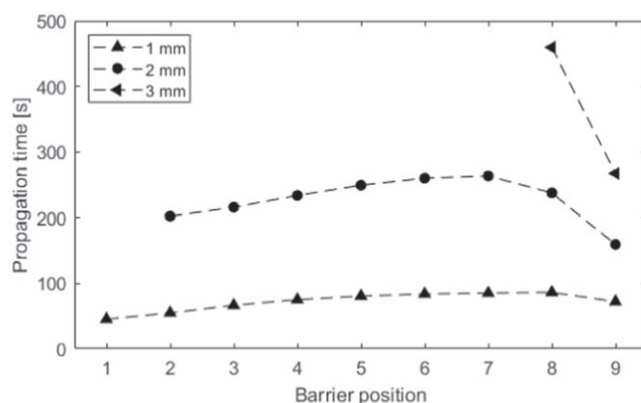


Figure 5. Influence of the barrier position on the propagation time in the liquid cooled setup. Barrier thickness is 1 mm, 2mm or 3 mm respectively and coolant flow rate is 1.21 min^{-1} . A missing data point indicates that the barrier stopped thermal propagation.

Further, we can observe that with $h = 50 \text{ W m}^{-2} \text{ K}^{-1}$ the propagation time at position 2 is significantly higher than at position 3 which opposes the trend of an increasing propagation time with the barrier position up to the maximum at position 7. This can be attributed to the effect that the propagation time undergoes a sharp increase when the barrier thickness approaches the critical, thermal propagation stopping thickness which can be seen in Fig. 3.

For studying the effect of liquid cooling on thermal propagation, a cooling plate is added to the battery system. It contacts all battery cells and the insulation at the bottom. The setup is described in further detail in Section "Cooling system model" and displayed in Fig. 1. A heat sink is modeled which represents a liquid coolant flow within the cooling plate according to Section "Cooling system model". For this series of simulations, different barrier thicknesses of 1 mm, 2 mm and 3 mm are applied. Again, the dependence of propagation time on the barrier position is investigated. The coolant flow rate is set to $\dot{V}_c = 1.21 \text{ min}^{-1}$. Figure 5 shows the propagation time at different barrier positions in the liquid cooled setup.

In comparison with the results of the setup without cooling, shown in Fig. 2, the curves for 1 mm and 2 mm barriers appear similar, but overall the propagation times are shifted to higher values. They are increased on average by 8.3 s or 14.2% in the cases with 1 mm barriers and by 42.3 s or 22.7% in cases with 2 mm barriers which shows that the cooling system has a higher impact when the barriers are thicker. It proves that the cooling system on its own is barely able to mitigate thermal propagation since the

processes are too fast to remove a meaningful amount of heat from the system. The heat sink is limited by cooling system capacity itself as well as the thermal transport within the battery cells. By extending the delay between the thermal runaway of the cells, total heat removal is enhanced and becomes more momentous.

This is even more apparent in the simulation series with 3 mm barriers. Here, the bottom cooling plate allows the stoppage of thermal propagation up to position 7. That poses a significant improvement to the cases without cooling where the 3 mm barrier only holds up to position 3. At position 7 the propagation time is still massively increased by 117.2 s compared to the simulations without cooling. This indicates that the barrier thickness of 3 mm is still close to the critical barrier thickness in this case. However, at position 9, the increase in propagation time is relatively low at 27.4 s.

Further, the effect of the coolant flow rate on the propagation time was examined with two additional series of simulations. For one series, the flow rate was doubled to $\dot{V}_c = 2.4 \text{ l min}^{-1}$. In the other series, the flow rate is set to 0 which means that there is no heat sink and effectively, the only difference to the cases without cooling is the heat conducting bottom plate. This represents a scenario where the cooling system is out of order due to the thermal runaway circumstances. The results are displayed in Fig. 6.

The comparison of the curves for flow rates of 1.2 l min^{-1} and 2.4 l min^{-1} shows no significant difference between these two setups. On average, doubling the flow rate only increases the propagation time by 0.9 s. This indicates that the main bottleneck for heat removal from the system via bottom cooling is thermal transport within the battery rather than the capacity of the cooling system. Thus, the geometry of the battery cells and the placement of the cooling plates largely affects how well the cooling system supports the mitigation of thermal propagation. Fu et al. performed a simulation study on the effect of liquid side cooling on thermal propagation.¹⁹ In this study, the cooling plates were placed between the battery cells and significant impact on both mitigation and prevention was found. In comparison with our present work, this underlines the importance of the placement of cooling plates.

In the simulations with a cooling plate but no coolant flow, the lowest propagation times were found among all cases with 2 mm barriers. With increasing position number propagation times show a decreasing trend from 100.7 s at position 2 to 28.6 s at position 9. The reason is that the bottom plate poses an additional pathway for heat transfer which even bypasses the thermal barrier. Towards position 9, the bottom plate becomes the main pathway as it is heated by an increasing number of battery cells. This emphasizes the importance of preventing heat transfer through periphery components such as defect cooling systems or the housing which has not been included in this work when designing safety measures for battery packs. It is to be mentioned that propagation times were evaluated by the average temperature peaks instead of the gas generation in this simulation series since the gas generation peaks were blurred unlike in all other cases.

Impact of the confining pressure.—In our previous study, we investigated the effect of gas generation on the thermal transport during thermal runaway and thermal propagation processes²⁶ and found parameters for the gas thermal resistance model, described in Section "Battery properties", for different confining pressure values. These parameters are shown in Table VII.

The parameter sets are applied to the battery arrangement in order to investigate these thermal transport phenomena in a multi-cell environment. Figure 7 shows the propagation time curves over the barrier position for different confining pressures.

As a general trend, it is observable that the propagation time is diminished with lower pressure. This can be explained by the higher thermal resistance of produced gases. Due to the lower confining pressure, the battery cells expand further as gas is generated during the heating-up. That hinders the thermal transport and thus causes

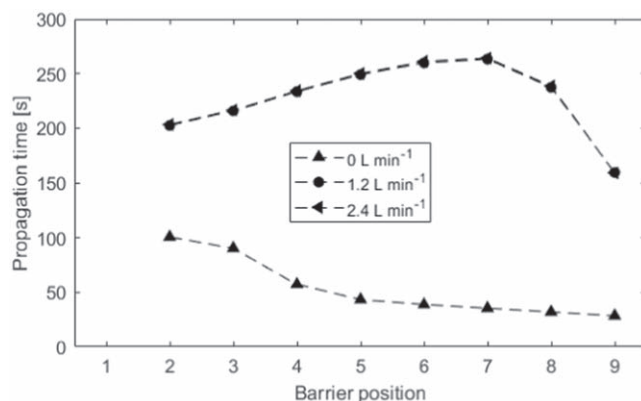


Figure 6. Dependence of the propagation time on the position of the thermal barrier in the liquid cooled setup with varying coolant flow rates. They range from 0 to 2.4 l min^{-1} . Barrier thickness equals 2 mm in all cases. A missing data point indicates that the barrier stopped thermal propagation.

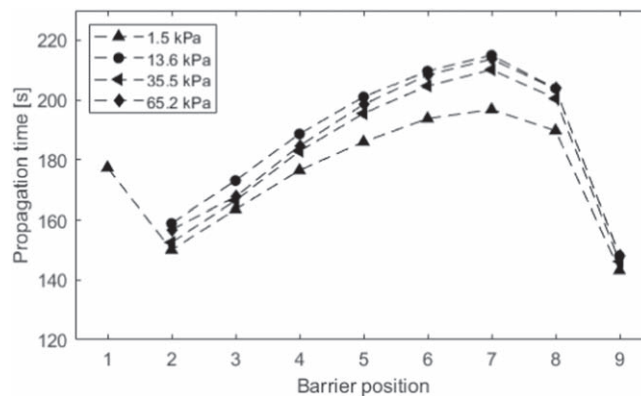


Figure 7. Influence of the confining pressure on the propagation time at different barrier positions. Confining pressure is regarded via the gas thermal resistance model. A missing data point indicates that the barrier stopped thermal propagation. Propagation was only stopped with barriers on position 1 and confining pressure above 1.5 kPa.

Table VII. Parameters of the gas thermal resistance model in dependence on the confining pressure.²⁶

Confining pressure [kPa]	$n_{\text{gas, Vent}}$ [mol kg ⁻¹]	$R_{\text{gas, max}}$ [m ² K W ⁻¹]	$R_{\text{gas, 3}}$ [m ² K W ⁻¹]
1.5	0.1473	0.1686	0.0564
13.6	0.1473	0.1045	0.0219
35.5	0.1473	0.1140	0.0135
65.2	0.1473	0.1017	0.0090

heat to accumulate faster in the cell behind the barrier, leading into a lower propagation time. The simulation series with a confining pressure of 13.6 kPa poses an outlier to this trend as it yields the highest propagation times despite having the third highest pressure applied. Looking at the parameters of the gas thermal resistance model in Table VII, the value of $R_{\text{gas, max}}$ is significantly lower than the trend of decreasing thermal resistance of gases with increasing confining pressure would suggest. This may be an experimental artifact.²⁶ We can conclude that the low value of $R_{\text{gas, max}}$ combined with the high value of $R_{\text{gas, 3}}$ leads into the highest propagation times.

This results in this Section are, however, opposed to the findings in our previous study where an increased pressing force led into a shorter propagation time.²⁶ The reason was a different setup with

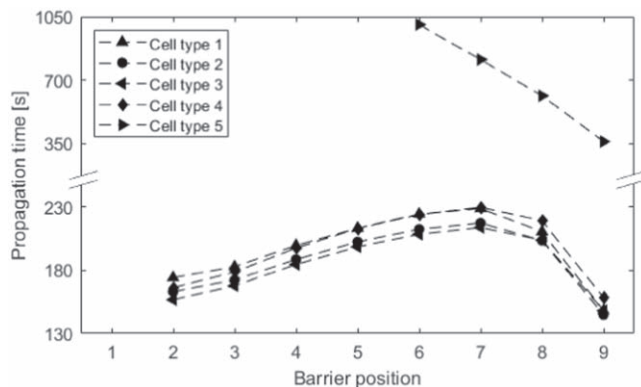


Figure 8. Propagation times at different barrier positions for the five cell types, ranging from high energy to high power cells. Barrier thickness is kept at 2 mm throughout all trials. A missing data point indicates that the barrier stopped thermal propagation.

multiple thermal barriers which already caused heat accumulation and preheating effects of the cell behind the barrier caused the propagation time to be diminished. This underlines the importance of considering all surrounding parts and boundary conditions when evaluating thermal propagation since some parameters may have different effects depending on the environment.

Influence of cell properties on thermal propagation.—In order to assess thermal propagation behavior of various cell types, simulations were conducted using the cell data given in Table IV. The inner buildup parameters are not measured data from real cells but represent the typical trends of fewer, thicker electrodes with lower porosity for cells with higher energy density within a reasonable value range.^{42,43} Cell type 3 is the reference which was used for all previous sections. Again, these simulations were conducted with barriers at the nine different positions and the barrier thickness is 2 mm. Since the packing density of cells in the battery system has not been changed throughout these simulation series, the pack level energy density only depends on cell properties given in Table IV.

Figure 8 shows the results of the simulations with different cell types. It is apparent that with the high power cell type 5, the highest propagation times are yielded. Due to the relatively low amount of active material, heat release during thermal runaway is lower than it is with the other cell types. Therefore, the 2 mm barrier is already enough to fully stop thermal propagation up to position 5 and is close to the critical thickness at positions 6 to 9 which causes the high propagation times up to 1007 s. However, the differences in propagation time are relatively low between the other four cell types. The main reason for that is reactant depletion. Since electrolyte solvent is part of the main heat releasing reactions on the anode (R1) and cathode (R4 and R5) side, its consumption limits thermal runaway heat release. Reactant depletion, especially of electrolyte solvent, is also reported by Shurtz et al. to limit thermal runaway heat release.^{29,39} Further, it is in accordance with experimental results by Ohneseit et al.⁴⁷ who showed that energy density has no clear impact on thermal runaway behavior if the cell chemistry is the same.

However, some differences among cell types 1 to 4 are still apparent. Overall, cell types 2 and 3 have the highest specific heat release which reflects in the fastest thermal propagation. This can be explained by two contrary effects. In cells of type 4 the heat release is limited by the lower amount of active material. Cells of type 1 have a high amount of excess active material that does not react due to solvent depletion. This causes an increased thermal mass and thus a lower specific heat release. Another potential difference in thermal propagation behavior between high energy and high power may arise from the differing particle sizes. Shurtz et al. report a rise in reaction rates of active material decomposition reaction with increasing active material surface which result from a lower particle size.⁴⁸

Conclusions

In this work, a previously developed thermal runaway and propagation model is applied on an exemplary battery system in order to investigate on general effects of arrangement, cooling systems, confining pressure and cell types.

In the ten cell reference system, series of simulations were performed with only one or two thermal barriers. Heat generation by thermal runaway reactions, heat capacity and dissipation are major influences on the critical, thermal propagation stopping barrier thickness. Additionally, it was found that pre-heating and heat accumulation effects significantly impact critical barrier thickness and also propagation time in case that thermal propagation cannot be stopped. Based on these results, the following recommendations for pack designers can be derived:

- With a given total space for thermal insulation, it is more effective to use fewer but thicker barriers rather than many thin barriers. The dependence of the propagation time on the barrier thickness is approximately quadratic over a wide range. Therefore, total propagation time will be longer with few, thick barriers if thermal propagation cannot be avoided. Additionally, thick barriers are more likely to stop propagation completely.
- Heat accumulation is to be avoided. Cells on the rim of the battery pack are prone to this if heat dissipation on the boundary is insufficient. More importantly, this also means that too many barriers negatively affect propagation prevention as they amplify heat accumulation, which is shown by the simulation series with two thermal barriers. Again, this underlines that few thick barriers are to be recommended over many thin barriers with the same total volume.
- Cooling systems must be considered when designing the safety system. However, synergy with thermal barriers is needed to achieve a significant effect in hazardous situations because heat transport limitations within the battery cells restrict heat dissipation through the cooling systems. This is particularly salient in the liquid edge cooled battery packs since the enhanced heat dissipation only affects one side of the stack. For optimal effect on propagation prevention, short battery internal heat transfer paths to the heat sinks should be striven for. Thicker barriers enhance the time for heat dissipation and thus the effect of cooling systems on thermal propagation.
- Heat transfer paths that bypass the safety insulations have to be prevented. This was showcased by simulating a defect bottom cooling system with no coolant flow which diminished propagation times harshly. It is also valid for other potential bypasses like metal housings.
- Battery properties need to be assessed thoroughly as they largely affect thermal runaway and propagation behavior. Besides cell chemistry, this also includes the inner buildup of the cells. Reactant depletion effects must be considered as they may lead into non-intuitive results.

Overall, we have demonstrated that thermal propagation in battery stacks cannot simply be described by the thermal runaway behavior of single cells and the insulation properties. Especially heat transfer and accumulation phenomena are of major importance as well. For pack designers, this implies that the entire battery system including peripheral components has to be regarded when designing the safety system. Thermal propagation experiments are insufficient to prove the effectiveness of potential thermal propagation countermeasures unless the thermal surroundings are carefully reproduced. They may however serve as calibration for modeling approaches.

Acknowledgments

This work was funded by the Baden-Württemberg Ministry of Science, Research and the Arts (grant number 32-7533-4-161.2/9/12) and the Federal Ministry of Education and Research (grant number 03XP0369A) within the project “AgiloBat” as part of the Innovation Campus Mobility of the Future. The research was also supported by the state of Baden-Württemberg through bwHPC.

ORCID

Niklas Weber  <https://orcid.org/0009-0009-9154-9114>

References

- S. Gao, L. Lu, M. Ouyang, Y. Duan, X. Zhu, C. Xu, B. Ng, N. Kamyab, R. E. White, and P. T. Coman, *J. Electrochem. Soc.*, **166**, A2065 (2019).
- S. Gao, X. Feng, L. Lu, N. Kamyab, J. Du, P. Coman, R. E. White, and M. Ouyang, *International Journal of Heat and Mass Transfer*, **135**, 93 (2019).
- C. F. Lopez, J. A. Jeevarajan, and P. P. Mukherjee, *J. Electrochem. Soc.*, **162**, A1905 (2015).
- UNECE Draft global technical regulation on electric vehicle safety. <http://www.unece.org/fileadmin/DAM/trans/doc/2017/wp29grsp/ECE-TRANS-WP29-GRSP-2017-02e.docx>. Accessed: 2024-09-20.
- S. Arora, W. Shen, and A. Kapoor, *Renew. Sustain. Energy Rev.*, **60**, 1319 (2016).
- C. Yuan, Q. Wang, Y. Wang, and Y. Zhao, *Applied Thermal Engineering*, **153**, 39 (2019).
- F. Liu, J. Wang, N. Yang, F. Wang, Y. Chen, D. Lu, H. Liu, Q. Du, X. Ren, and M. Shi, *Energy*, **257**, 124768 (2022).
- X. Rui, X. Feng, H. Wang, H. Yang, Y. Zhang, M. Wan, Y. Wei, and M. Ouyang, *Applied Thermal Engineering*, **199**, 117521 (2021).
- S. Chavan, B. Venkateswarlu, R. Prabakaran, M. Salman, S. W. Joo, G. S. Choi, and S. C. Kim, *Journal of Energy Storage*, **72**, 108569 (2023).
- Q. Wang, B. Jiang, B. Li, and Y. Yan, *Renew. Sustain. Energy Rev.*, **64**, 106 (2016).
- D. Werner, S. Paarmann, A. Wiebelt, and T. Wetzel, *Batteries*, **6**, 13 (2020).
- D. Werner, S. Paarmann, A. Wiebelt, and T. Wetzel, *Batteries*, **6**, 12 (2020).
- D. Chen, J. Jiang, G. H. Kim, C. Yang, and A. Pesaran, *Applied Thermal Engineering*, **94**, 846 (2016).
- M. Shahjalal, T. Shams, M. E. Islam, W. Alam, M. Modak, S. B. Hossain, V. Ramadesigan, M. R. Ahmed, H. Ahmed, and A. Iqbal, *Journal of Energy Storage*, **39**, 102518 (2021).
- S. Xin, C. Wang, and H. Xi, *Applied Thermal Engineering*, **224**, 120100 (2023).
- C. Roe et al., *Journal of Power Sources*, **525**, 231094 (2022).
- M. Suresh Patil, J. H. Seo, and M. Y. Lee, *Energy Conversion and Management*, **229**, 113715 (2021).
- Y. Deng, C. E. J. Feng, H. Zhu, J. Chen, M. Wen, and H. Yin, *Applied Thermal Engineering*, **142**, 10 (2018).
- H. Fu, J. Wang, L. Li, J. Gong, and X. Wang, *Applied Thermal Engineering*, **234**, 121349 (2023).
- K. S. Kshetrimayum, Y. G. Yoon, H. R. Gye, and C. J. Lee, *Applied Thermal Engineering*, **159**, 113797 (2019).
- J. Lamb, C. J. Orendorff, L. A. M. Steele, and S. W. Spangler, *Journal of Power Sources*, **283**, 517 (2015).
- A. Kvasha, C. Gutiérrez, U. Osa, I. de Meatza, J. A. Blazquez, H. Macicior, and I. Urdampilleta, *Energy*, **159**, 547 (2018).
- C. Forestier, A. Lecocq, A. Zantman, S. Grugeon, L. Sannier, G. Marlair, and S. Laruelle, *J. Electrochem. Soc.*, **167**, 090513 (2020).
- R. K. Daniels and A. Prabhakar, *Journal of Energy Storage*, **72**, 108191 (2023).
- N. Weber, S. Schuhmann, J. Tübke, and H. Nirschl, *Energy Technology*, **11**, 2300565 (2023).
- N. Weber, S. Schuhmann, R. Löwe, J. Tübke, and H. Nirschl, *Energy Adv.*, **3**, 1697 (2024).
- R. Spotnitz and J. Franklin, *Journal of Power Sources*, **113**, 81 (2003).
- J. C. Hewson, H. Zhou, M. Parmananda, R. C. Shurtz, and P. P. Mukherjee, *MRS Bull.*, **46**, 402 (2021).
- R. C. Shurtz, J. D. Engerer, and J. C. Hewson, *J. Electrochem. Soc.*, **165**, A3878 (2018).
- J. Lamb, C. J. Orendorff, E. P. Roth, and J. Langendorf, *J. Electrochem. Soc.*, **162**, A2131 (2015).
- S. E. Sloop, J. K. Pugh, S. Wang, J. B. Kerr, and K. Kinoshita, *Electrochem. Solid-State Lett.*, **4**, A42 (2001).
- O. Haik, S. Ganin, G. Gershinsky, E. Zinigrad, B. Markovsky, D. Aurbach, and I. Halalay, *J. Electrochem. Soc.*, **158**, A913 (2011).
- F. Larsson, P. Andersson, P. Blomqvist, and B. E. Mellander, *Sci. Rep.*, **7**, 10018 (2017).
- P. Ribière, S. Grugeon, M. Morcrette, S. Boyanov, S. Laruelle, and G. Marlair, *Energy Environ. Sci.*, **5**, 5271 (2012).
- J. Liu, S. Yadav, M. Salman, S. Chavan, and S. C. Kim, *International Journal of Heat and Mass Transfer*, **218**, 124748 (2024).
- M. M. Ghahremanpour, P. J. Van Maaren, J. C. Ditz, R. Lindh, and D. Van der Spoel, *The Journal of Chemical Physics*, **145**, 114305 (2016).
- K. Gavritchev, G. Sharpataya, A. Smagin, E. Malyi, and V. Matyukha, *Journal of Thermal Analysis and Calorimetry*, **73**, 71 (2003).
- G. K. Johnson, R. T. Grow, and W. N. Hubbard, *The Journal of Chemical Thermodynamics*, **7**, 781 (1975).
- R. C. Shurtz, *J. Electrochem. Soc.*, **167**, 140544 (2020).
- R. C. Shurtz and J. C. Hewson, *J. Electrochem. Soc.*, **167**, 090543 (2020).
- Nist chemistry webbook database <https://webbook.nist.gov/cgi/> accessed: 2022-06-25.
- S. Yu, S. Kim, T. Y. Kim, J. H. Nam, and W. I. Cho, *Journal of Applied Electrochemistry*, **43**, 253 (2013).
- Y. H. Chen, C. W. Wang, X. Zhang, and A. Sastry, *Journal of Power Sources*, **195**, 2851 (2010).
- M. G. Jeong, J. H. Cho, and B. J. Lee, *Journal of Power Sources*, **424**, 35 (2019).
- Z. Huang, H. Wang, T. Yang, W. Tian, T. Dong, and J. Wu, *Applied Thermal Engineering*, **217**, 119255 (2022).
- X. Feng, X. He, M. Ouyang, L. Lu, P. Wu, C. Kulp, and S. Prasser, *Applied Energy*, **154**, 74 (2015).
- S. Ohneseit, P. Finster, C. Floras, N. Lubenau, N. Uhlmann, H. J. Seifert, and C. Ziebert, *Batteries*, **9**, 237 (2023).
- R. C. Shurtz, J. D. Engerer, and J. C. Hewson, *J. Electrochem. Soc.*, **165**, A3891 (2018).